


Article

3D Sedimentary Architecture of Sandy Braided River, Based on Outcrop, Unmanned Aerial Vehicle and Ground Penetrating Radar Data

Wei Guo ^{1,2,*} , Chunmei Dong ^{1,2}, Chengyan Lin ^{1,2}, Tao Zhang ³, Zhongxiang Zhao ⁴ and Jia Li ^{1,2}

¹ School of Geosciences, China University of Petroleum, Qingdao 266580, China; lcydcm@upc.edu.cn (C.D.); ycmsycdz@126.com (C.L.); b14010012@s.upc.edu.cn (J.L.)

² Key Laboratory of Deep Oil and Gas, China University of Petroleum, Qingdao 266580, China

³ College of Earth Science and Engineering, Shandong University of Science and Technology, Qingdao 266590, China; zhangt1982@sdust.edu.cn

⁴ School of Geosciences, Yangtze University, Wuhan 430100, China; zhaozhongxiang5@163.com

* Correspondence: guowei8829@126.com; Tel.: +86-186-6394-8829

Abstract: Ground Penetrating Radar (GPR) is a geophysical method that uses antennas to transmit and receive high-frequency electromagnetic waves to detect the properties and distribution of materials in media. In this paper, geological observation, UAV detection and GPR technology are combined to study the recent sediments of the Yungang braided river study area in Datong. The application of the GPR technique to the description of fluvial facies and reservoir architecture and the development of geological models are discussed. The process of GPR detection technology and application includes three parts: GPR data acquisition, data processing and integrated interpretation of GPR data. The geological surface at different depths and scales can be identified by using different combinations of frequencies and antenna configurations during acquisition. Based on outcrop observation and lithofacies analysis, the Yandong Member of the Middle Jurassic Yungang Formation in the Datong Basin has been identified as a typical sandy braided river sedimentary system. The sandy braided river sandbody changes rapidly laterally, and the spatial distribution and internal structure of the reservoir are very complex, which has a very important impact on the migration and distribution of oil and gas as a reservoir. It is very important to make clear the characteristics of each architectural unit of the fluvial sand body and quantitatively characterize them. The architectural elements of the braided river sedimentary reservoir in the Datong-Yungang area can be divided into three types: Channel unit, bar unit and overbank assemblages. The geological radar response characteristics of different types of sedimentary units are summarized and their interfaces are identified. The channel sediments form a lens-shaped wave reflection with a flat at the top and convex-down at the bottom in the radar profile, and the angles of the radar reflection directional axes are different on both sides of the sedimentary interface. In the radar profile, the deposit of the unit bar is an upward convex reflection structure. The overbank siltation shows a weak amplitude parallel reflection structure. The flood plain sediments are distributed continuously and stably in the radar profile, showing weak reflection characteristics. Different sedimentary units are identified by GPR data and combined with Unmanned Aerial Vehicle (UAV) detection data, and the establishment of the field outcrop geological model is completed. The development pattern of the diara is clarified, and the swing and migration of the channel in different stages are identified.

Keywords: sandy braided river; diara deposits; composite bar; geological model



Citation: Guo, W.; Dong, C.; Lin, C.; Zhang, T.; Zhao, Z.; Li, J. 3D Sedimentary Architecture of Sandy Braided River, Based on Outcrop, Unmanned Aerial Vehicle and Ground Penetrating Radar Data. *Minerals* **2022**, *12*, 739. <https://doi.org/10.3390/min12060739>

Academic Editor: Ricardo Ferreira Louro Silva

Received: 5 May 2022

Accepted: 7 June 2022

Published: 10 June 2022

Publisher's Note: MDPI stays neutral with regard to jurisdictional claims in published maps and institutional affiliations.



Copyright: © 2022 by the authors. Licensee MDPI, Basel, Switzerland. This article is an open access article distributed under the terms and conditions of the Creative Commons Attribution (CC BY) license (<https://creativecommons.org/licenses/by/4.0/>).

1. Introduction

In the past 20 years, two-dimensional (2D) outcrop images have been used because of the limitations of one-dimensional data (profile observations, lithological descriptions, and drilling data) in reconstructing the depositional systems architecture [1]. The facies

model of the outcrop, combined with porosity and permeability data, indicates reliable sedimentological and stratigraphic details and can be used to characterize the subsurface reservoir in 3D [2]. The use of ground penetrating radar (GPR) is a new technology for characterizing sedimentary rocks in three dimensions [3,4]. GPR is a high-resolution geophysical detection technology that can detect the internal material properties and distribution law of shallow underground rock units. The vertical resolution of GPR is several decimeters, and the penetration depth is several meters to tens of meters. GPR systems acquire the spatial distribution of electrical properties of shallow subsurface rocks by transmitting and receiving high-frequency electromagnetic waves (typically in the range of 50–900 MHz) through antennas. According to the buried depth and size of the target geological body, it is necessary to select GPR antennas with different frequencies, and the antenna frequency range is generally from 50 MHz to 900 MHz. The attenuation of the GPR signal is determined by the maximum penetration depth and is inversely proportional to the resistivity. The wave velocity and attenuation of high-frequency electromagnetic waves are determined by the apparent dielectric constant of the underground medium.

Similar to the interpretation of large-scale stratigraphic sequences from seismic data, GPR data have great potential to describe architectural elements in different sedimentary environments [5]. Unlike conventional seismic data, which have a vertical and horizontal resolution of no more than 10 and 30 m, the vertical resolution of GPR for sedimentary structures can reach 10 cm, which is necessary to describe and interpret depositional paleoenvironments. So far, GPR surveys have been applied to recently unconsolidated sediments but not too consolidated sedimentary sequences where petroleum accumulations have occurred [6]. In a near-surface environment, the attenuation of the GPR signal will be accelerated due to water-bearing formations. GPR detection is carried out in an arid environment, the electromagnetic wave attenuation is slow, and the stratum in the study area does not contain water. The electrical properties of consolidated rocks are affected by diagenesis, faulting and weathering of exposed outcrops. The original sedimentary response is superimposed on these factors, which interferes with the response waveform of GPR. Pre-processing, background removal, deconvolution and depth migration can focus the GPR image to the target interval and reduce artefacts unrelated to the original lithology.

In this study, the vertical resolution of the 200 MHz GPR data is 0.1 m, and the penetration depth is about 7.5 m, which can be used to study the sedimentary structure and interior detail of the outcrop. The vertical resolution of the 200 MHz GPR data is better, approximately 0.2–0.3 m, but the penetration depth is about 8–10 m due to strong signal attenuation. Most of the interpretation in this study was done on the migrated 200 MHz GPR data, as the outcrop is about 6 m thick above the ground.

GPR data are usually composed of 2D profiles [7] or orthogonal with the large spacing of 2D measuring lines interpolated into a pseudo-3D grid [8–10], for example the GPR measurements of the Switzerland recent-delta gravels [11] and the Utah Cretaceous shoreface sandstone bodies. If the attenuation and dispersion of the signal are not considered, the GPR data and the seismic reflection data are different in scale, and the same processing method can be used. This means that many of the processing techniques, and methods to interpret 3D seismic data can be used for 3D GPR surveys. For example, GPR data are acquired on a 3D grid, and the horizontal and vertical resolution of the 3D GPR data is improved by migration.

GPR has been successfully applied in a variety of clastic sedimentary environments [12–15] to resolve high-precision imaging of the geometry and interior of architectural elements and bedforms [11,16–18]. In this study, the interfaces of different architectural elements are mapped according to 2D GPR profiles (100 and 200 MHz). In the GPR sections, most of the sedimentary structural interfaces can be responded to on the GPR profile. A dense grid of high-resolution GPR profiles (200 MHz) was obtained and interpolated into 3D GPR data. Although the process of data acquisition and processing of high-resolution 3D GPR is more complex and time-consuming, the display of results is more detailed, and the accuracy of the geological model is also increased [9,19].

2. Geologic Setting

The study outcrop area is located in the Datong Basin in northwest China. The eastern and southern margins of the basin are major faults, and the northern and western boundaries edges are denuded. The present tectonic framework of the basin is the result of the late Indosinian movements [20]. The basin developed over 200 m of Lower Jurassic braided river deposits in unconformable contact with the underlying Paleozoic marine strata and is overlain by Middle to Upper Jurassic lacustrine deposits [21]. The fluvial deposits in the studied outcrop area are located between the mountain range in the northwest and the lacustrine basin in the southeast, and the braided river extends from the alluvial fan to the middle of the basin, 20 km away from the northwest mountain range and more than 100 km away from the southeast lake [22]. The Yungang Formation is divided into three lithologic members, which are the Conglomerate Member, the Rockcave Member and the Mudstone Member from bottom to top [21,22]. The Conglomerate Member contains grey conglomerate intercalated sandstone, with a thickness of less than 40 m. The Rockcave Member comprises red coarse sandstone and a small amount of red mudstone. The Mudstone Member is dominated by variegated mudstone with a small amount of fine-sandstone layers (Figure 1). Overall, the structure and color of the strata indicate that the paleoclimate of the Middle Jurassic was dominated by a semi-arid to arid climate [20,22]. The sections that were cut by road used in this study are mainly exposed in the Yungang Formation Rockcave Member, with a total thickness of more than 60 m and an exposed thickness of fewer than 30 m. The lithology of the Rockcave Member is medium- or coarse-sandstone, with a small amount of gravel and mud in the form of lag deposits at the bottom of the sandstone body. There is a small amount of mudstone in the large-scale sandstone layers, and the sedimentary structure is mainly trough and tabular cross-bedding [23]. Large trough-like cross-bedding is common, and without obvious internal lamination inside that, the sedimentation rate is high and is accompanied by channel migration. Planar cross-bedding represents lateral and downstream accretion and is the fundamental unit of channel deposition. Within the study area, an east-west railway runs perpendicular to the paleo-current direction, crosses six adjacent braided sandbars, and cuts them.

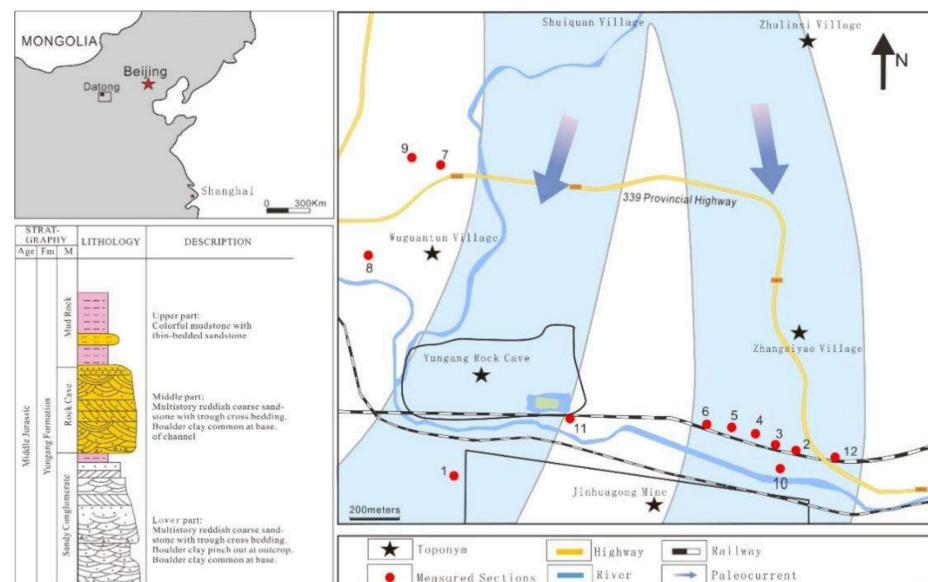


Figure 1. Location of Datong Basin, the regional geological background of outcrop and lithologic column of exposed Rockcave Member [19].

3. Methods and Data

Traditional outcrop research is mainly based on profile observation, primarily focusing on the description of the sedimentary structure and reservoir structure (Figure 2). In

addition to the observation of outcrop profiles, UAV mapping and GPR detection were also used in this study (Figure 3).

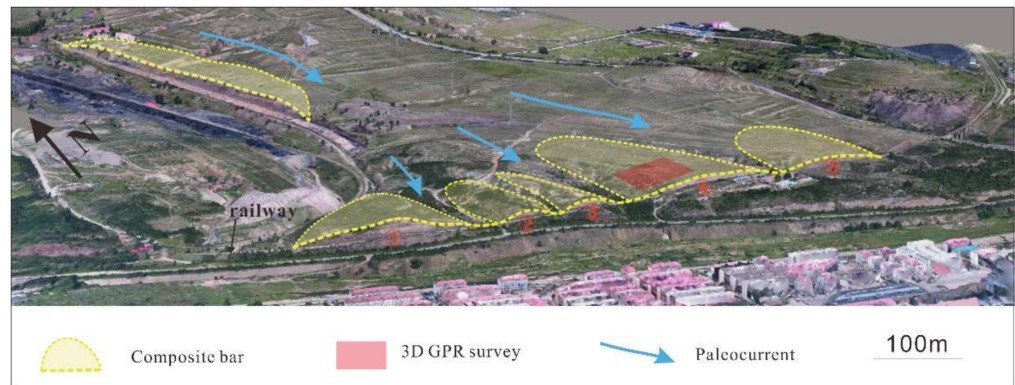


Figure 2. UAV aerial photos. Five compound bars cut by the railway can be identified, and there is a large pro-provenance channel bar section in the north. 3D GPR survey on the No.4 composite bar, 34×45 m in size.

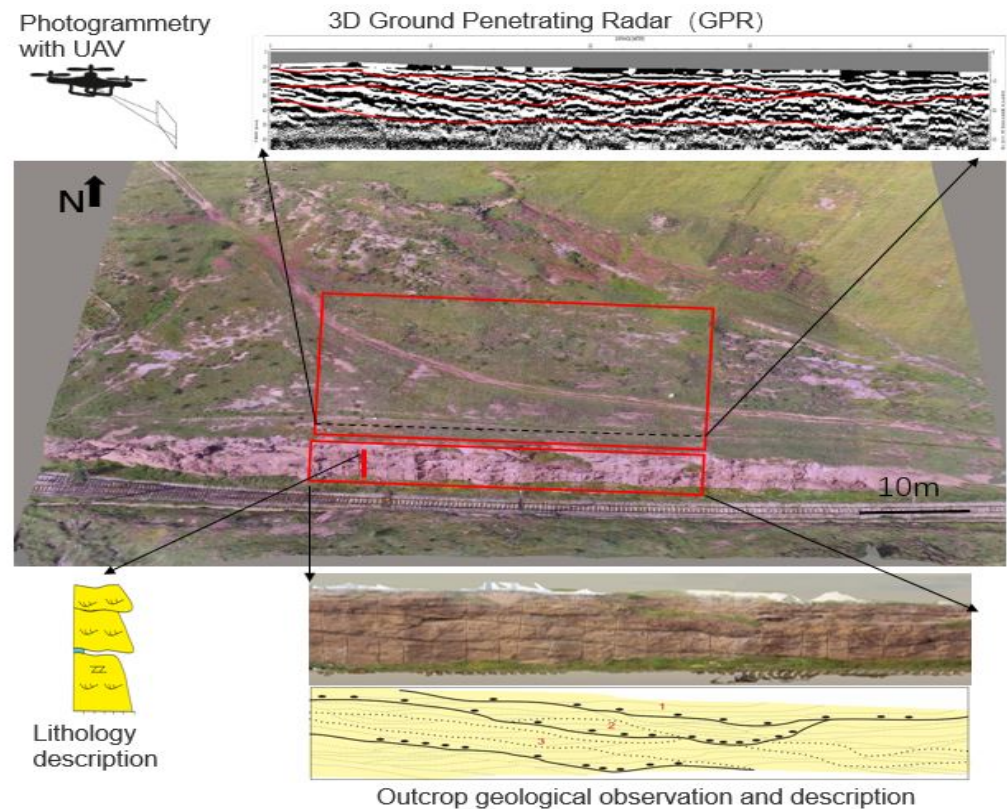


Figure 3. This study applies to the workflow and methods for outcrops, including outcrop observation and description, lithologic assemblage description, ground penetrating radar detection and UAV aerial photography.

3.1. Profile Observation and Petrophysical Parameters Test

Through the profile observation of the outcrop, the thickness, contact relationship and geometric shape of different sedimentary units on the profile, as well as the details of sedimentary structure types and lithological information can be obtained. Our goal was to explore the sedimentary process and further characterize the sedimentary facies.

In this study, 13 samples from different parts of the profile were also taken, and their dielectric constant was tested, which can provide important parameters for GPR data processing.

3.2. UAV Mapping

The high-resolution photos provided by UAV mapping can identify a variety of information, such as stratigraphic profiles, coordinate information and elevation data.

The DJI Phantom 4 Pro UAV platform with a CMOS camera was used in this study. The maximum flight altitude of a UAV is 110 m relative to the terrain. The sensor size is 23.5×15.7 mm with 20 million effective pixels. The UAV camera system mapped a total area of 2.4471 km² of terrain and 12 outcrop profiles (Figure 1). The virtual outcrop model used Pix4D, a professional software designed for drone-based mapping, to establish a 3D landform model with a resolution of 5 cm.

3.3. GPR Detection

GPR is an efficient geophysical detection technology that can be used to characterize the surface and sedimentary structure of geological bodies in outcrop studies. Like the traditional seismic exploration, it is divided into three aspects: Data acquisition, signal processing and comprehensive interpretation.

3.3.1. Acquisition of GPR Data

In this study, five outcrop profiles were selected for GPR detection, with a total line length of 1221 m, including four two-dimensional GPR measuring lines and one high-resolution three-dimensional GPR survey. The GSSI (Geophysical Survey Systems, Inc., St. Nashua, NH, USA) SIR-3000 Ground Penetrating Radar system with 100 MHz and 200 MHz shielded antennas were used for this study. At Outcrop No.3, No.5, No.6 and No.8, GPR profiles of 50, 71, 62 and 248 m in length, respectively, were acquired with the 200 MHz shielded antenna that the penetration depth can reach 7.5 m below the surface, which can provide high-resolution images of the internal structure of the geological body. On the No.4 composite bar, which is relatively flat at the top, three-dimensional GPR detection was designed. The survey size was 45×34 m, and the number of measured lines was 10 in the east-west direction and 11 in the north-south direction. The grid spacing was 5 m in the east-west direction and 3.4 m in the north-south direction. GPR detection requires a relatively flat ground to ensure good coupling between the radar antenna and the ground and to acquire a high signal-to-noise ratio data.

3.3.2. GPR Data Processing

The purpose of GPR data processing is to suppress the interference and improve the signal-to-noise ratio and the resolution of the reflected wave. The reflection wave parameters (such as waveform, amplitude, etc.) extracted by data processing provide a guarantee for further geological interpretation. The GPR data processing workflow is shown in Figure 4.

The electromagnetic wave velocity of the sample was measured between 0.081 and 0.107 m/ns.

3.3.3. Interpretation of GPR Data

Similar to seismic in oil and gas exploration, interpretation of GPR data is based primarily on reflector patterns, using radar facies to analyze rock formations in the underground medium [19,24,25]. The interface and internal structure of a geological body are interpreted in terms of the amplitude, configuration, and continuity of the reflector and its external geometry [26–28]. There have been many successful cases of GPR in various clastic depositional environments, and it is capable of solving geometric problems at the scale of architectural elements and bedforms. The vertical resolution of GPR data in outcrop detection is the one-quarter wavelength. The reflection wavelength of GPR is calculated

according to Equation (1). The dielectric constant is measured by sandstone samples from the outcrop section, and the average value is 4.08. The longitudinal resolution of the 100 and 200 MHz GPR data is 36 and 14 cm, respectively.

$$\lambda = \frac{C}{f\sqrt{\epsilon}} \quad (1)$$

where ϵ represents relative permittivity (measured value 4.08), f is the antenna frequency in Hz, and C is the speed of light in a vacuum with a value of 3×10^8 m/s.

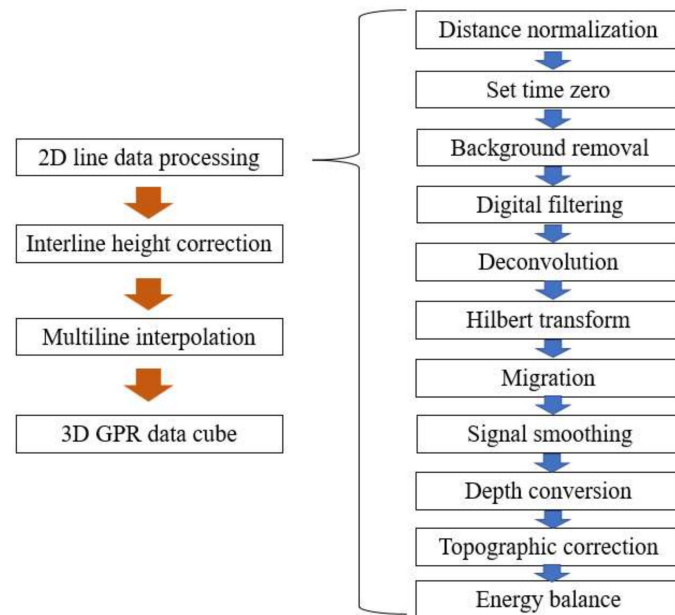


Figure 4. In this study, the GPR data processing process and 3D interpolation applied.

In this study, the 2D GPR profiles (100 and 200 MHz) were mapped to geological interpretations that could be compared to the outcrop profiles. Most of the sedimentary units can be well identified from GPR sections. The high-resolution 3D GPR profile grid (200 MHz) is more complex to process and interpret, but the data are far more detailed and reliable, which is helpful for further geological model building.

4. Results

4.1. Architectural Elements

Architectural elements refer to the shape, scale, direction and superposition relationship of different levels of constituent units. The fluvial reservoir architecture elements depend on the related strata [29] and the depositional products of sedimentary processes [30,31]. In this study, the features of the sedimentary architecture are controlled by the bed form and boundary of the channel. The description of braided river sedimentary architectural elements based on outcrop observation and the previous division scheme are shown in Table 1 [13,21,29,32–37]. Architectural elements can be divided into three types: Channel unit, bar unit and overbank assemblages. The channel unit includes a filling channel unit (CHf) and a migration channel unit (CHm). The bar unit consists of unit-bar (UB) elements and compound-bar (CB) elements. The non-channel part is mainly composed of the overbank assemblage (OF) consisting of interfluvial muddy and sandy splays. In the channel belts, different sedimentary units in the channel belt have experienced different sedimentary processes.

Table 1. Classification of architectural elements of braided river system by different researchers.

Architectural Element	Reference
channels; slip-bounded bars; sand flats; flood plains	Cant and Walker 1978 [34]
simple or compound bars; tabular sandstone; down-climbing bar; small-scale channel; large-scale channel; laterally accreted bar; sandstone ridges; tabular mudstone	Allen 1983 [33]
channel; lateral accretion; sediment gravity flow; gravel bar; sand bedform; downstream accretion; laminated sand; overbank fines	Miall 1985 [31]
simple bars; transitional dune-bar; dune complexes; downstream accretion; channel (sandstone); channel (mudstone)	Hjellbakk 1997 [36]
large channel fills; small channel fills; unit bar; compound bar; flood plain	Bridge and Lunt 2006 [37]

4.1.1. Filling Channels (CHf)

Sediments in the filling channel are mainly medium-grained sandstones (St, Sl and Fl) with minor cross-bedding. Smaller mudstone intraclasts sediments occur as lag deposits at the bottom of the filling channel. Sediments filling the channel are often structureless or laminated, and the grain size decreases gradually upward. The thickness of the filling channel is 1.2–3.4 m, the width is often more than 30 m, the average width-thickness ratio is 17.6, and the width-thickness ratio indicates that the lateral migration capacity of the channel is relatively weak. A large number of trough cross-beds are developed in the filling channel, and their widths are measured to be 0.18 to 4.63 m, with an average of 1.54 m. The cross-bed thickness ranges from 0.03 to 0.38 m, with an average of 0.21 m. The width-thickness ratio of cross-beds is 5.9–19.5, averaging 12.3. The average width-thickness ratio of the trough cross-beds is relatively high, which indicates that the incising ability of the channel is relatively weak [38]. The relatively small size of the trough cross-beds indicates that the energy of the paleocurrent is relatively low, so fine-grained sediments are widely developed in this element [39]. The low gradient of the W/T trend along the channel (0.0147) indicates that the channel flows energy is uniform. Abandoned channels are also developed in the filling channels [40], which are filled by layered, fine-grained muddy sediments and often develop on the flanks of a channel belt. It is formed because the upstream end of the compound bar blocks the flow due to channel diversion, and the fine-grained sediments are deposited due to the static flow. Abandoned channels may also be developed in mudstone-sandstone mixed filling channels. [41].

4.1.2. Migrating Channels (CHm)

The grain size of the migrating channel is mainly medium to coarse sandstone and gradually decreases upward. Large-scale trough stratification (St) developed in the unidirectionally inclined bedform and shows asymmetric characteristics (Figure 5). Channel bedforms were eroded and superimposed unidirectionally in one direction. The channel bases were incised into lower strata and the bed-forms bottom contains lags of mudstone intraclast. The thickness of the migrating channel element is between 0.38 and 5.96 m, with an average of 3.13 m. The width is between 13 and 131 m, with an average of 59.5 m. The average width-to-thickness ratio is 21.8. The average width, thickness and width-thickness ratio of the trough cross-bed developed in the migrating channel are 1.52, 0.16 and 9.26 m, respectively. The outer geometry of the migrating channel is asymmetric because of the lateral migration of the channel caused by unilateral accretion on the channel bedforms [42]. The scale of the channel and sedimentary structures may indicate that the hydrodynamic energy is moderate and therefore the channel is less capable of erosion. The average width-to-thickness ratio of St is higher than that of the switching channel, indicating the decrease of the bed-form incision. The lateral migration bed-forms of the channel with unilateral aggradation usually occur near the compound bar, which is located near the channel boundary with high sinuosity and can extend laterally for tens of meters [43].

However, due to the frequent occurrence of erosion and bifurcation in the braided channel, migration channels are less common.

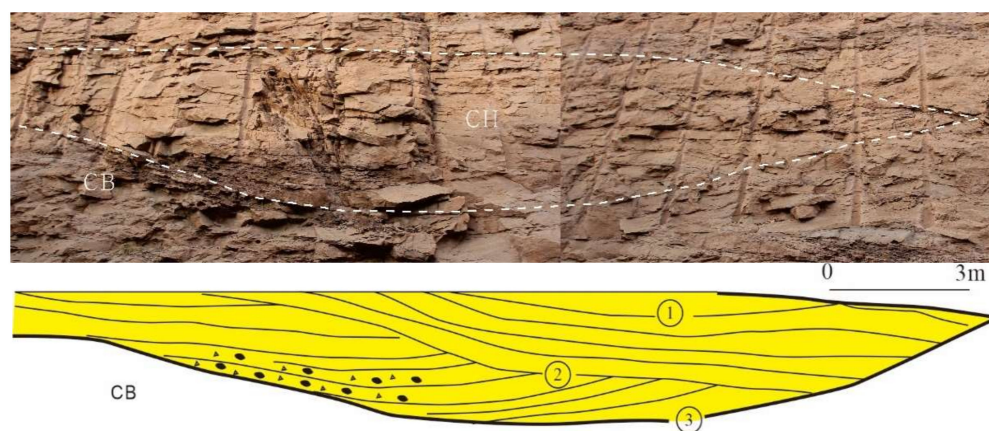


Figure 5. The typical channel architecture elements of the outcrop section of the Yungang Formation include a filling channel and unilateral accretion migration channel. ①, ② and ③ represent the shape of the river bottom in different periods.

4.1.3. Unit Bar (UB)

The simple bar of Hjellbakk [36] is considered the unit dam (UB) in this study, with grain size being medium-coarse sandstone and decreasing gradually toward the top, and parallel bedding (Sp) and ripple cross-bedding (Sr) is developed. Large cross-beddings also tend to have high dips. The thickness of the unit bar is between 0.8 and 5.3 m, and the width can reach tens of meters. The base is generally an erosion surface, and the top contacts are convex-up. Such element was often formed during a single, relatively continuous flow, which is the reason for the occurrence of a single set of planar cross-beds. Under the condition of increasing flow velocity, the coalesced dunes were formed on inclined high-dip strata [44]. With the increase of sediment concentration and the decrease of water depth over the top of the bar (resulting in the decrease in flow velocity), isolated growth cores are formed on the low-relief bar [45]. Various cross-bedding structures are formed on the top of the sand bar, resulting in another rapid and short-term flow velocity fluctuation [46,47]. Therefore, in the channel belt, and when the hydrodynamic energy change increases, the unit bars were greatly transformed, so there was an erosion surface in front of the bar. A large number of plane cross-bedded groups developed in the unit bars, which combined with other architectural elements to form composite bars.

4.1.4. Compound Bar (CB)

The composite bar (CB) element is the high-quality reservoir in braided river deposits, and the main lithological assemblages are plane stratification (Sp), horizontal stratification (Sh), and minor trough stratification (St) or ripple sand (Sr) in the upper segment. This usually consists of multiple lower-order elements (downstream-accretive (DA), transverse-accretive (LA), unit-bar (UB), or chute) (Figure 6). As can be observed from the white dotted line in Figure 6, there is usually gravel or mud erosion at the bottom of CBs [44]. From the outcrop, it can be observed that the grain size of the element decreases gradually upward, and the thickness of the cross-beds also decreases gradually upward. With the decrease of hydrodynamic energy, the grain size shows an upward trend of fining in the CB. The thickness of CBs is usually more than 10 m, and the width is tens of meters. According to HjellBakk [36], at the bottom of the wide and flat channel, these sediments are deposited by local accumulation and gradually increase, which is consistent with the convex-up external configuration of typical dune complexes. The chutes developed at the top of the unit bar or the composite bar and may evolve into new channels during the flood period. Subsequently, large compound bars formed during periods of high flow and were eroded by chutes or

channels into several oblique bars during the low-flow stage. The tabular cross-beds in the bar unit show various bedform geometries and stacking patterns, which are indicative of various depositional processes. The width, thickness and dip angle (α) of the cross-beds of the bar units in the outcrop section were measured to characterize them. The width of single-set planar cross-beds is 0.24–7.35 m, with an average of 3.42 m. The thickness of single-set planar cross-beds is 0.07–2.61 m, with an average of 1.14 m. The dip angle α of single-set planar cross-beds is 7–22°, with an average of 12°. Since the scale of cross-beds is consistent with the depth of channel flow [48], the scale of cross-bedding is determined by the flow depth at which various bedforms and bounding surfaces formed in braided fluvial channels and vary frequently. The thickness of the planar cross-bedding is relatively large at the bottom of the bar and gradually decreases upward, which indicates that the hydrodynamic force also decreases gradually during the vertical accretion of bedforms. The thickness of cross-beds is positively correlated with the dip angle. Therefore, when the water level is high, the bottom of the composite dam develops thick high-angle large-scale cross-beds, and when the water level drops, the bottom of the composite bars develop thin cross-bedding with a low dip angle.

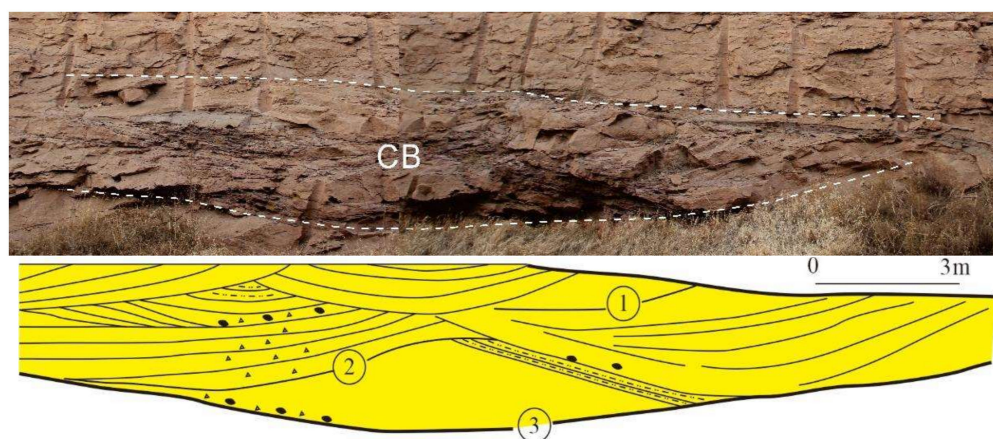


Figure 6. The typical composite bar architecture elements of the outcrop section of the Yungang Formation. The composite bar element comprises unit bars and chutes. ①, ②, and ③ represent channel bottom shapes of different periods, respectively.

4.1.5. Overbank Fines (OF)

The overbank fine-grained (OF) deposits mainly consist of massive mudstone (Fm) and laminated mudstone (F1), with thin interbeds of fine sandstone (S1) (Figure 7). The clay content gradually increases upward and is covered by other sandy architectural elements. The sediments are mainly purple or red mudstone, with little or no pedogenic development. The mudstone layer has a thickness of 0.06 to 2.1 m and a width of several meters to more than 100 m. A few fine roots were found in the upper part of the mudstone layer, and no other fossils or bioturbation were found.

The sedimentary structure formed by overbank muddy deposits in the floodplain is laminated mudstone (F1), and the sandy crevasse splays during the flood period are thin, fine-grained sandstone. Abandoned channels in the upper part of the channel elements in the channel belt form massive mudstones (Fm). The red color of the laminated mudstone generally indicates good drainage conditions [49], the high clay content in the mudstone and the presence of a lesser amount of sandstone in the upper part of this element indicating that the fluvial system may hinder the discharge of rainwater and seasonal floods [50]. These fine-grained sediments are often developed at the top of the channel and are filled with floodplain sediment as the water level rises above the bank of the channels [51].

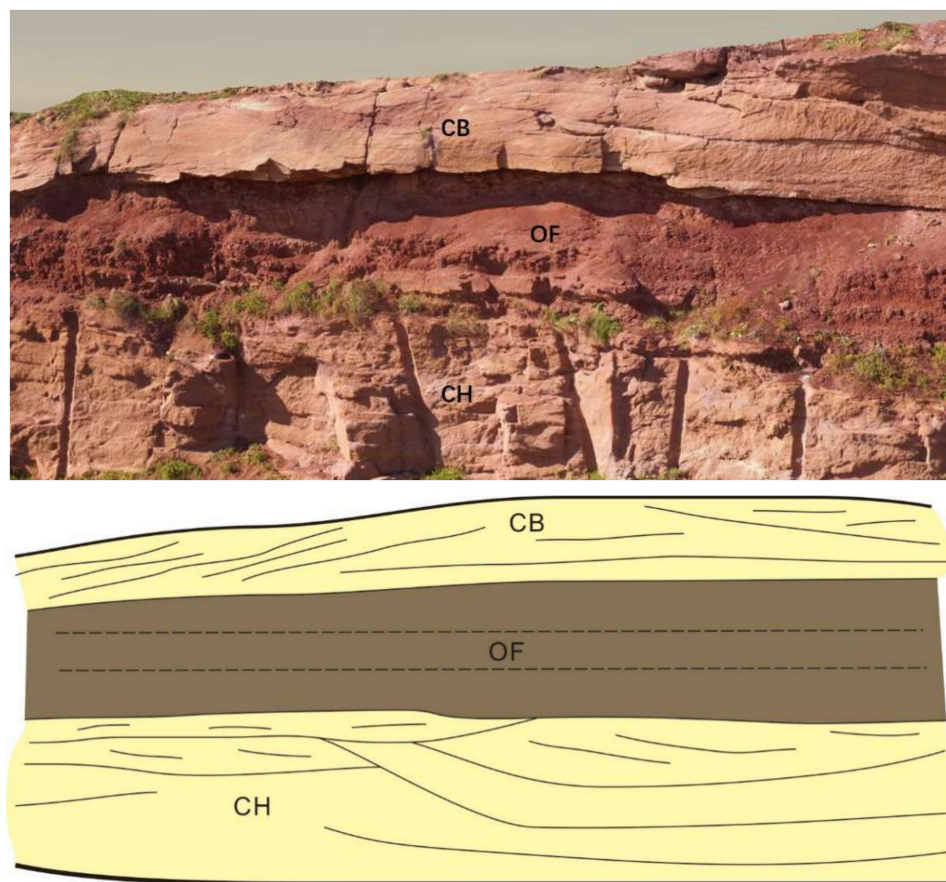


Figure 7. Typical bank overflow deposits in the outcrop section of the Yungang Formation. The grain size is mudstone and siltstone. Occurs on channel deposits.

4.2. GPR Radar Facies

Outcrop No.4 is a large compound bar in which the river channel, unit bar and other architectural elements can be identified. The reflection structure in the 200 MHz GPR profile corresponds well to the architectural elements in the outcrop profile and can further depict its internal structure (Figure 8).

A 3D GPR survey grid was acquired on Outcrop No. 4, and a shielded 200 MHz antenna was adopted. The penetration depth of the GPR electromagnetic wave was about 10 m below the surface (Figure 9). The survey measuring line number was 10 in the east-west direction and 11 in the south-north direction, the total survey size was 45×34 m, and the track pitch was 5 m in the east-west direction and 3.4 m in the south-north direction.

GPR profiles of the composite bar exhibit parallel or subparallel reflectors with large amplitudes and local high dips on the outcrop. Near the southern section, imbricated reflection structures are seen inside the channel, indicating that the channel is offset and has a transverse relationship to the unit column, while near the northern section, multiple superimposed S-shaped reflection patterns are seen across the GPR section (Figure 10). This shows the westward migration of the channel. There is an obvious protruding radar phase in the unit bar on the east side of the section. In the direction of the provenance, the channel can be seen cutting downward, and the compound strip is accreted downward.

The 3D GPR geological body was obtained by Kriging interpolation of the 2D GPR lines high corrected by interlines (Figure 11). The channel migration and the vertical accretion of the unit bar can be observed from the 3D GPR data volume. A clear S-shaped reflection structure (black dotted line) can be seen at the head of the unit bar.

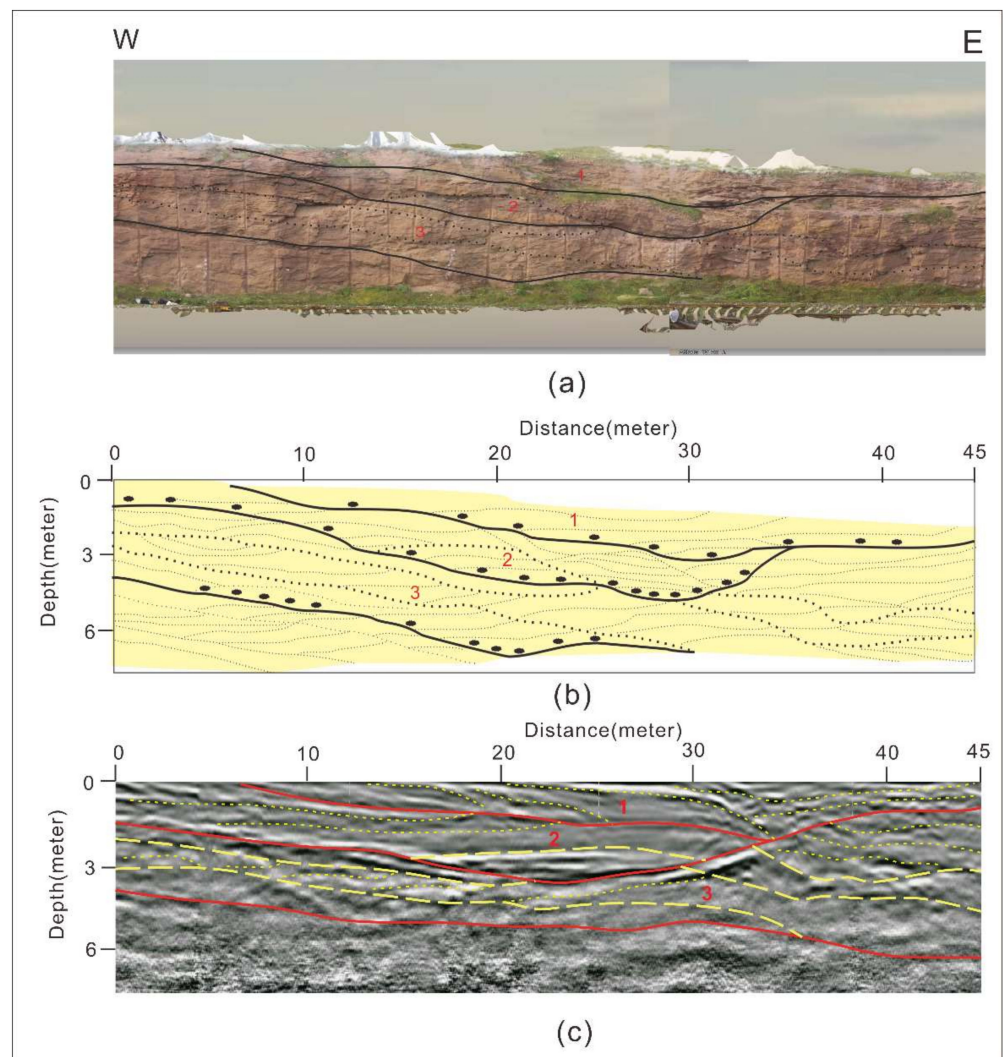


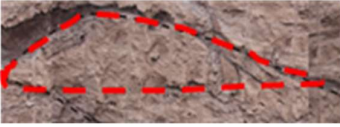

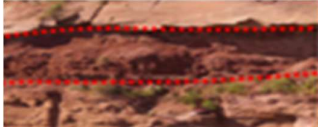
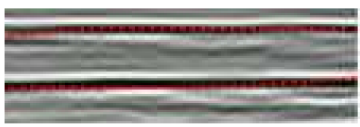


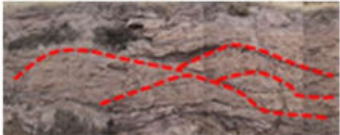
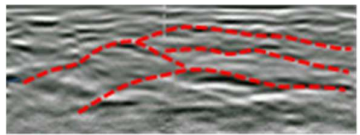




Figure 8. UAV photograph of Outcrop No. 4 with corresponding geological sketch and ground-penetrating radar profile. The section length is 45 m and the thickness is 8 m. 1, 2 and 3 represent different periods. The frequency of the radar antenna is 200 MHz, which can identify the spatial distribution of the main architectural elements and internal structures in the outcrop. (a) The outcrop profile; (b) Geological sketch map, black dots indicate gravel; (c) GPR profile. The lithology of the channel deposit in the outcrop study area is generally sandstone, with a small amount of gravel at the bottom, and the overall grain size is coarse. On the GPR profile, the geometric shape of the waveform is lenticular with a flat top and convex-down bottom, the events in the channel are parallel or sub-parallel, and there are different reflection responses on both sides of the interface. The deposit of the unit bar was relatively coarse-grained, mainly composed of sandstone, sometimes containing gravel, and developed abundant bedding. The radar profile shows lenticular reflection with a flat bottom and convex-up top, and the internal reflection is relatively chaotic. The overbank deposit occurs under relatively quiet water conditions, and the deposition process is relatively slow and steady. The grain size of the sediment is small, and the sediment is clay and silt. The GPR profile shows a parallel reflection structure with weak amplitude (Table 2). The GPR facies features identified in the observable profile and compared with the geological features in the outcrop profile can be used to interpret 3D radar data.

Table 2. Summary of identified sedimentary architectural elements and their GPR characteristics in the Yungang Formation, Datong Basin.

Element	Facie Composition	Outcrop Pictures	GPR Features
Filling Channels	St, Sp, Sm, Sh, Sl, Sr		
Unit Bar	Sp, St, Sr		
Over Bank	Fm, Fl		
Migrating Channels	St, Sp, Sm, Sh, Sl, Sr		
Compound Bar	Sp, St, Sr		
Abandoned channel	Fm		

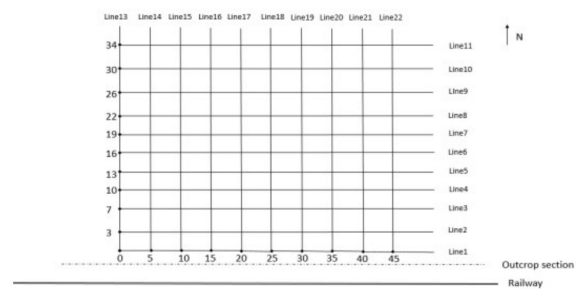
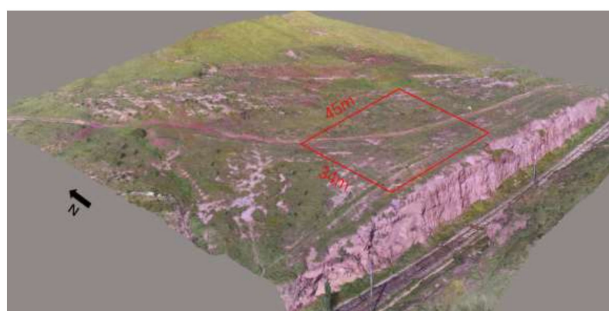


Figure 9. The 3D GPR survey grid of Outcrop No. 4. The size is 45 × 34 m, and the track pitch is 5 m in the X direction and 3.4 m in the Y direction.

GPR reflections correlate well with interfaces between sandstone layers and mudstone layers within mudstone up to 10 m below ground because there are significant variations in the electrical properties of the rocks on either side of these interfaces. Mudstone layers are characterized by irregularity in thickness and shape and appear as discontinuous and irregular reflections in GPR profiles (Figure 10). Using the GPR data with a 200 MHz antenna, many layers significantly smaller than 0.3 m cannot be resolved (Figure 11).

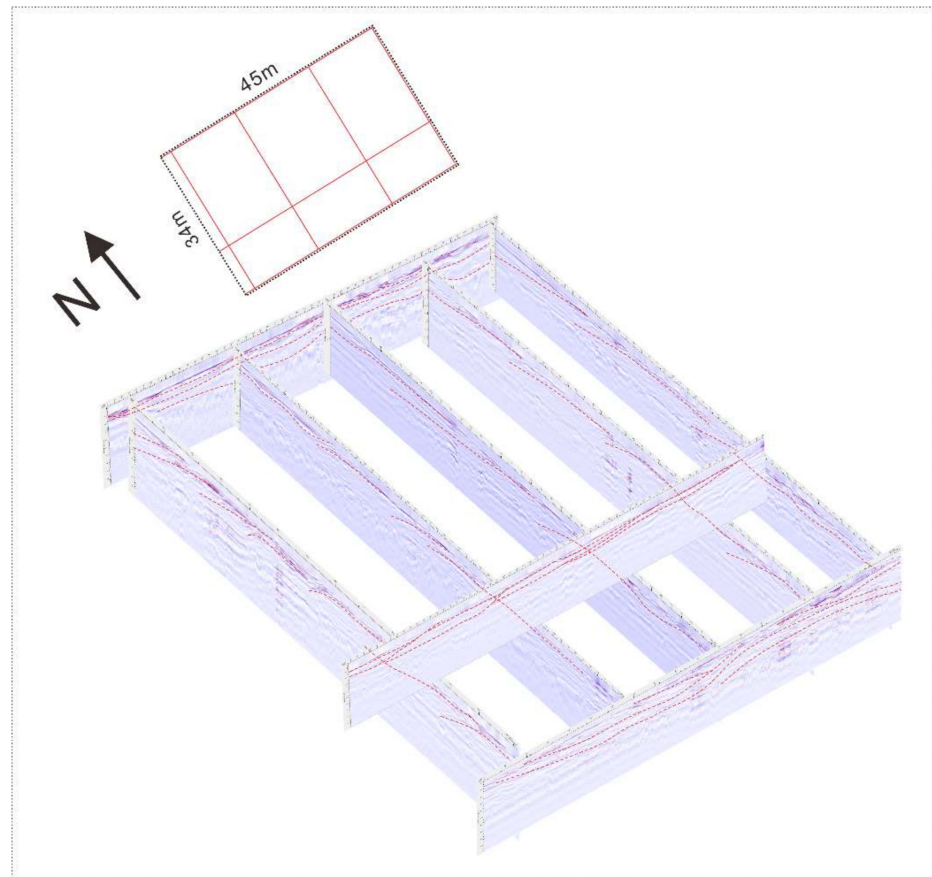


Figure 10. GPR network 2D profile grid.

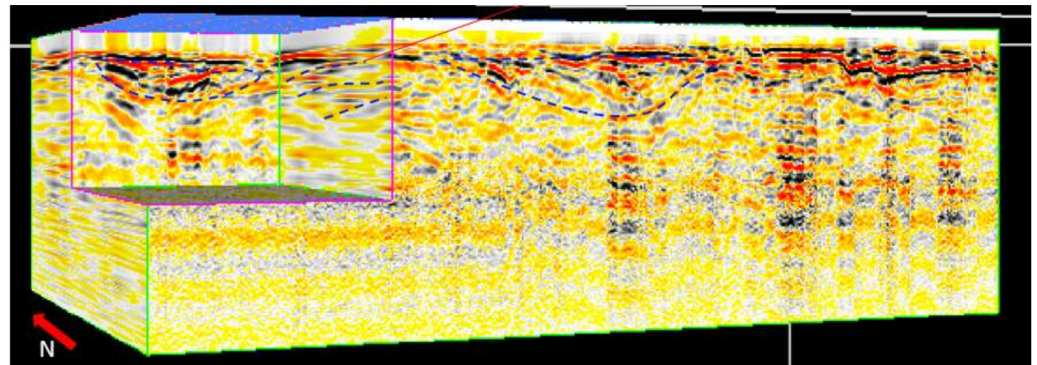


Figure 11. The GPR 3D data with dimensions of $45 \times 34 \times 10$ m. The migrating channels and the forward accretion of the unit bar can be observed. The GPR profile of the bar head reflects the sigmoidal stratification identified.

5. Discussion

5.1. Sedimentary Stage of Sandy Braided River

Through the GPR 3D data volume, three third-order boundary surfaces of 1.2.3 are interpreted, which respectively represent the bedform of the channel in different periods (Figure 12). Sandy braided river deposits can be divided into four stages: Erosion stage, development stage, stable stage and abandonment stage (Figure 13).

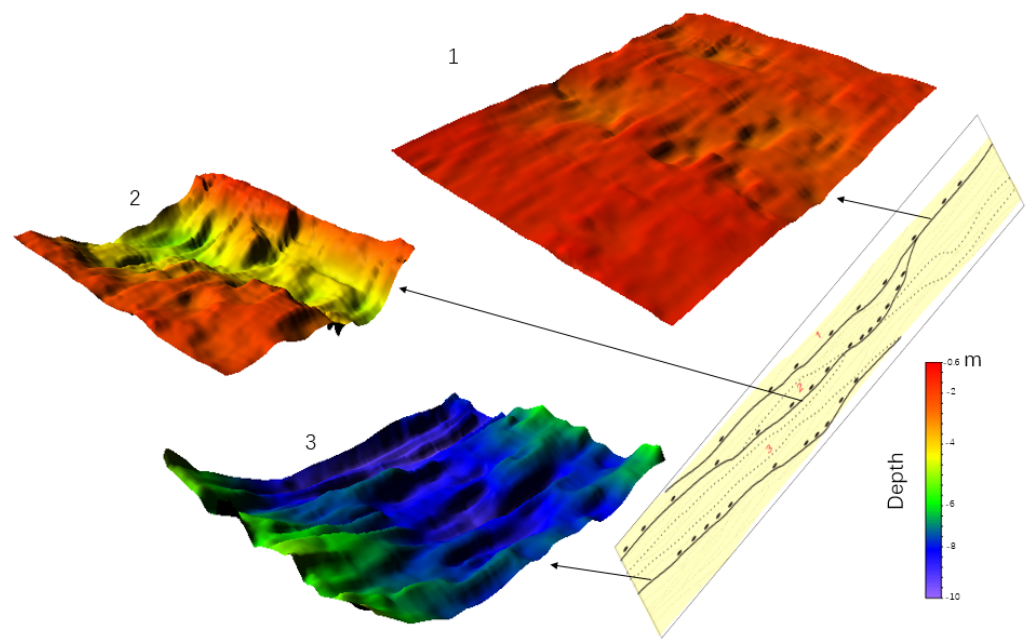


Figure 12. Delineation of the three surfaces in Figure 7 using GPR 3D data. 1, 2, 3 represent channel bottom shape of different periods, respectively.

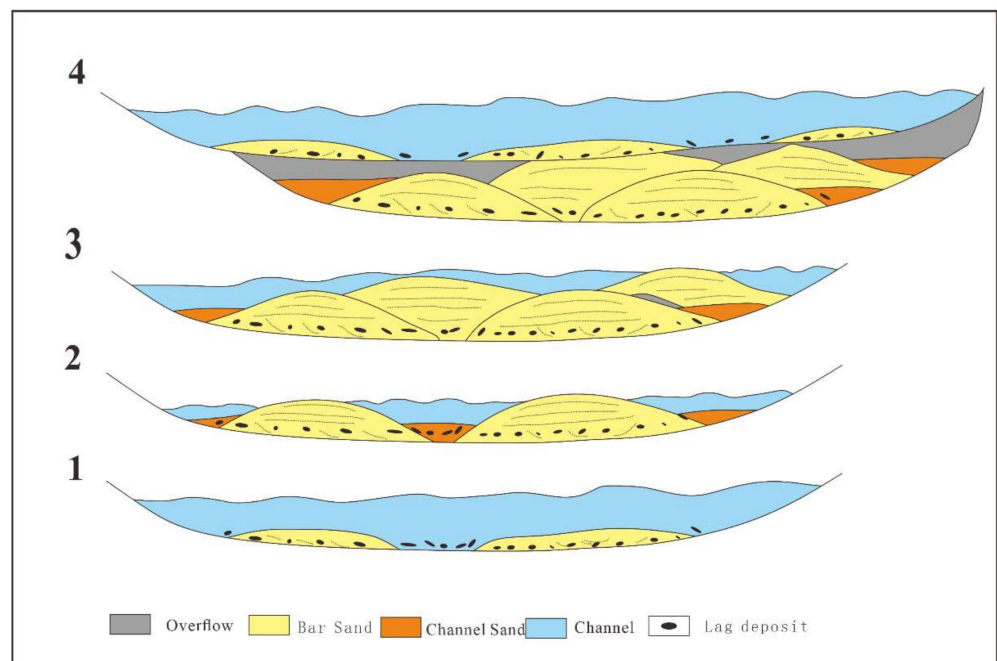


Figure 13. Depositional process of the sandy braided river of Yungang Formation in Datong Basin. 1, 2, 3, 4 indicate the stages of depositional process.

In the early stage of channel sedimentation, the mudstone is washed and stirred by the rapid flow to form mud gravel, which is the lag sediment deposited at the bottom of the bar and channel [49]. Later, the braided river deposits are developed on interface 3, and the unit bar is formed in the channel. The sedimentary structure is mainly trough and tabular cross-bedding, and the grain size is medium to coarse sandstone. The braided channels on both sides of the unit bar are developed and filled. The bedform of the channel formed after the completion of the development stage is Interface 2. Above surface 2, due to the swing migration of water flow, the channel will migrate and change its course, and the early channel will be abandoned, forming a new channel and a new bar. At this stage,

several migration-type and erosion-type composite sand bars are formed [50]. The vertical direction is a positive rhythmic combination pattern showing the upward fining of grain size in multiple periods. After the formation of the compound bar, the bedform of the river channel is interface 1. With the weakening of hydrodynamic force, the scale of the river channel gradually decreases and small-scale sand bars are deposited [51]. Sedimentary structures in the upper part of the channel are mainly low-angle inclined bedding and horizontal bedding, while the lithology is dominated by medium-fine sandstone or siltstone. As the hydrodynamics continue to weaken, the channel is gradually filled and abandoned by fine-grained sediments and floodplain mudstone brought by floods.

5.2. Establishment of Outcrop Geological Model

Through the above analysis of the sedimentary model of the sandy braided river, and combined with the virtual outcrop model obtained by UAV detection, the outcrop geological model was established (Figure 14). The scale of the model is 1.5 km in the east-west direction and 2 km in the north-south direction. In consideration of the paleogeomorphology and sedimentary structure style, the paleocurrent direction is approximately from north to south. The model is also based on the three interfaces 1, 2 and 3. The model can show the various architectural elements in the braided river deposits and the smaller-scale sedimentary structures within them. The model can identify and describe the heterogeneity of the architectural elements in the sandy braided river system, such as the variation of permeability.

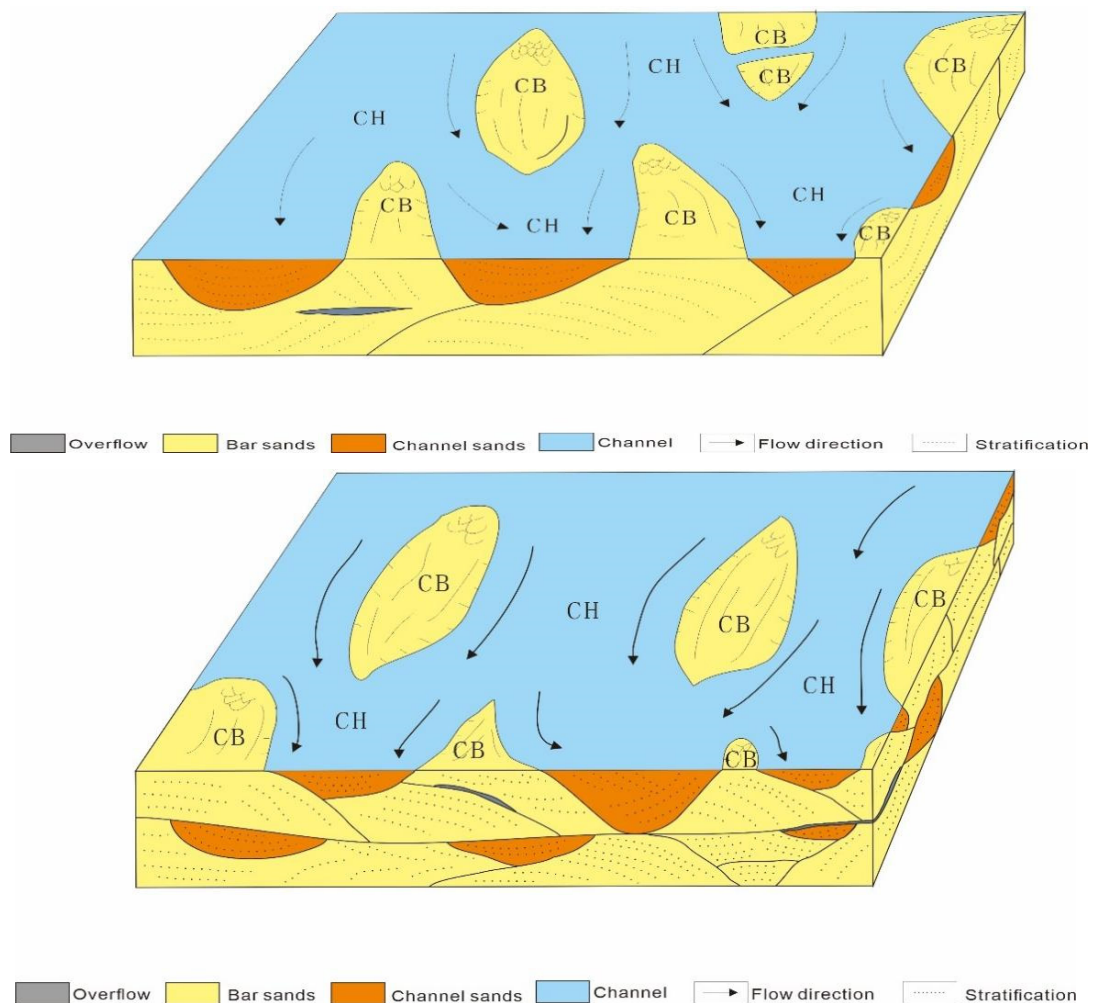


Figure 14. Cont.

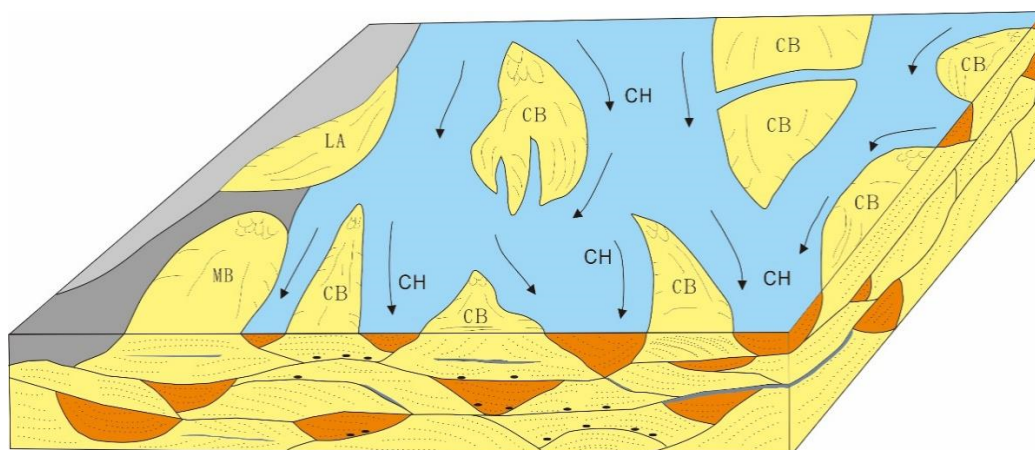


Figure 14. The three periods of the sedimentary model of the Yungang Formation in the Datong Basin outcrops area.

6. Conclusions

Based on 3D GPR data, detailed sedimentary and stratigraphic information and UAV detection results, the braided river architecture units and internal sedimentary elements in Datong Basin were identified and analyzed. GPR is a geophysical method that uses antennas to transmit and receive high-frequency electromagnetic waves to detect the properties and distribution of materials in media. The same structural elements and boundary surfaces were interpreted in the offset GPR data.

The interfaces of different architectural elements were mapped according to 2D GPR profiles (100 or 200 MHz). Most of the sedimentary structural interfaces can be responded to on the GPR profile. A dense grid of high-resolution GPR profiles (200 MHz) was obtained to interpolate image selected sites into 3D.

The vertical resolution of the 200 MHz GPR data is about 0.2–0.3 m, but the penetration depth is about 8–10 m due to strong signal attenuation. Most of the interpretation in this study was done on the migrated 200 MHz GPR data, as the outcrop is about 6 m thick above the ground

The architectural elements in the study area are determined by the internal lithofacies combination and genetic characteristics of the sedimentary unit and the geometric shape of the external sedimentary structure. Architectural elements can be divided into three categories: Channel unit, bar unit and overbank assemblages. The channel unit includes a filling channel unit (CHf) and a migration channel unit (CHm). The bar unit consists of unit-bar elements (UB) and compound-bar elements (CB). The non-channel part is mainly composed of the overbank assemblage (OF) consisting of interfluvial muddy and sandy splays. In the channel belts, each sedimentary unit represents a particular sedimentary process.

GPR profiles of composite bar exhibit parallel or subparallel reflectors with large amplitudes and local high dips on the outcrop. Near the south profile, an imbricated reflection structure can be observed inside the channel, indicating the migration of the channel and a lateral relationship with the unit bar, while near the north profile, the GPR profile shows several superimposed S-shaped reflection patterns, showing the migration of the channel to the west. Obvious convex-up radar facies can be seen inside the unit bar on the east side of the profile. In the direction of the provenance, the downcutting of the channel and the downstream accretion of the composite bar can be seen.

Sandy braided river deposits can be divided into four stages: Erosion stage, development stage, stable stage and abandonment stage.

The outcrop geological model can show the various architectural elements in the braided river deposits and the smaller-scale sedimentary structures within them. The

model can identify and describe the heterogeneity of the architectural elements in the sandy braided river system, such as the variation of permeability.

Due to the uneven surface during field outcrop detection, the coupling between the radar antenna and the surface is not good, which may affect the accuracy of radar detection.

Author Contributions: Conceptualization, W.G.; methodology, C.D.; software, W.G.; validation, C.L.; formal analysis, T.Z.; investigation, J.L.; resources, C.L.; data curation, W.G.; writing—original draft preparation, W.G.; writing—review and editing, C.D.; visualization, Z.Z.; project administration, C.L. All authors have read and agreed to the published version of the manuscript.

Funding: This research was funded by the Joint Fund Projects (No.U19B2006), Natural Science Foundation of China (Grant No. U19B200129 and 41672129), Fundamental Research Funds for the Central Universities (Grant No. 19CX02001A).

Institutional Review Board Statement: Not applicable.

Informed Consent Statement: Not applicable.

Acknowledgments: We express our appreciation to the CNOOC Shanghai Research Institute and Sensors and Software Inc. for GPR support. Many thanks to Chengyan Lin, Chunmei Dong and Xian-guo Zhang of the Shandong Province Key Laboratory of Reservoir Geology at the China University of Petroleum, who provided logistical help. We thank the Shandong Province Key Laboratory of Reservoir Geology for equipment support. Many thanks also to all the people involved in the project.

Conflicts of Interest: The authors declare no conflict of interest.

References

1. Gawthorpe, R.L.; Collier, R.E.L.; Alexander, J.; Leeder, M.; Bridge, J.S. Ground penetrating radar: Application to sandbody geometry and heterogeneity studies. In *Characterization of Fluvial and Aeolian Reservoirs*; North, C.P., Prosser, D.J., Eds.; Geological Society of London: London, UK, 1993; Volume 73, pp. 421–432.
2. Beres, M.; Green, A.; Huggenberger, P.; Horstmeyer, H. Mapping the architecture of glaciofluvial sediments with three-dimensional georadar. *Geology* **1995**, *23*, 1087–1090. [[CrossRef](#)]
3. Beauprêtre, S.; Manighetti, I.; Garambois, S.; Malavieille, J.; Dominguez, S. Stratigraphic architecture and fault offsets of alluvial terraces at Te Marua, Wellington fault, New Zealand, revealed by pseudo-3D GPR investigation. *J. Geophys. Res. Solid Earth* **2013**, *118*, 4564–4585. [[CrossRef](#)]
4. Egli, P.; Irving, J.; Lane, S. Characterization of subglacial marginal channels using 3-D analysis of high-density ground-penetrating radar data. *J. Glaciol.* **2021**, *67*, 759–772. [[CrossRef](#)]
5. Forte, E.; Santin, I.; Ponti, S.; Colucci, R.R.; Gutgesell, P.; Guglielmin, M. New insights in glaciers characterization by differential diagnosis integrating GPR and remote sensing techniques: A case study for the Eastern Gran Zebù glacier (Central Alps). *Remote Sens. Environ.* **2021**, *267*, 112715. [[CrossRef](#)]
6. Brandes, C.; Igel, J.; Loewer, M.; Tanner, D.C.; Lang, J.; Müller, K.; Winsemann, J. Visualisation and analysis of shear-deformation bands in unconsolidated Pleistocene sand using ground-penetrating radar: Implications for paleoseismological studies. *Sediment. Geol.* **2018**, *367*, 135–145. [[CrossRef](#)]
7. Carling, P.A.; Bristow, C.S.; Litvinov, A.S. Ground-penetrating radar stratigraphy and dynamics of megaflood gravel dunes. *J. Geol. Soc.* **2016**, *173*, 550–559. [[CrossRef](#)]
8. Okazaki, H.; Nakazato, H.; Kwak, Y. Application of high-frequency ground penetrating radar to the reconstruction of 3D sedimentary architecture in a flume model of a fluvial system. *Sediment. Geol.* **2013**, *293*, 21–29. [[CrossRef](#)]
9. Okazaki, H.; Kwak, Y.; Tamura, T. Depositional and erosional architectures of gravelly braid bar formed by a flood in the Abe River, central Japan, inferred from a three-dimensional ground-penetrating radar analysis. *Sediment. Geol.* **2015**, *324*, 32–46. [[CrossRef](#)]
10. Beres, M.; Huggenberger, P.; Green, A.G.; Horstmeyer, H. Using two- and three-dimensional georadar methods to characterize glaciofluvial architecture. *Sediment. Geol.* **1999**, *129*, 1–24. [[CrossRef](#)]
11. Franke, D.; Hornung, J.; Hinderer, M. A combined study of radar facies, lithofacies and three-dimensional architecture of an alpine alluvial fan (Illgraben fan, Switzerland). *Sedimentology* **2015**, *62*, 57–86. [[CrossRef](#)]
12. Fielding, C.R.; Alexander, J.; McDonald, R. Sedimentary facies from GPR surveys of the modern, upper Burdekin River of north Queensland, Australia: Consequences of extreme discharge fluctuations. In *Fluvial Sedimentology VI*; Smith, N.D., Rogers, J., Eds.; International Association of Sedimentologists Special Publication: Algiers, Algeria, 1999.
13. Jol, H.M.; Smith, D.G. Ground penetrating radar of northern lacustrine deltas. *Can. J. Earth Sci.* **1991**, *28*, 1939–1947. [[CrossRef](#)]
14. Neal, A. Ground-penetrating radar and its use in sedimentology: Principles, problems and progress. *Earth Sci. Rev.* **2004**, *66*, 261–330. [[CrossRef](#)]

15. Xueming, X.; Aiken, C.L.; Bhattacharya, J.P.; Corbeanu, R.M.; Nielsen, K.C.; McMechan, G.A.; Abdelsalam, M.G. Creating virtual 3-d outcrop. *Lead. Edge* **2000**, *19*, 197–202.
16. Van Wagoner, J.C.; Mitchum, R.M.; Campion, K.M.; Rahmanian, V.D. Siliciclastic sequence stratigraphy in well-logs, cores and outcrop. American Association of Petroleum Geologists. *Methods Explor. Ser.* **1990**, *7*, 1–55.
17. Kraus, M.J.; Gwinn, B. Facies and facies architecture of paleogene floodplain deposits, Willwood Formation, Bighorn Basin, Wyoming, USA. *Sediment. Geol.* **1997**, *114*, 33–54. [[CrossRef](#)]
18. Andrews, S.D.; Moreau, J.; Archer, S. Devonian lacustrine shore zone architecture: Giving perspective to cliff exposures with ground penetrating radar. *Sedimentology* **2016**, *63*, 2087–2105. [[CrossRef](#)]
19. Gautam, P.; Gupta, S.D. Uses of Green's function for enhancing the image resolution of Ground Penetrating Radar (GPR) data. *J. Appl. Geophys.* **2022**, *201*, 104621. [[CrossRef](#)]
20. Miall, A.D. Hierarchies of architectural units in terrigenous clastic rocks, and their relationship to sedimentation rate. In *The Three-Dimensional Facies Architecture of Terrigenous Clastic Sediments and Its Implications for Hydrocarbon Discovery and Recovery*; SEPM (Society for Sedimentary Geology): Tulsa, OK, USA, 1991.
21. Karušs, J.; Lamsters, K.; Ješkns, J.; Sobota, I.; Džeriņš, P. UAV and GPR Data Integration in Glacier Geometry Reconstruction: A Case Study from Irenebreen, Svalbard. *Remote Sens.* **2022**, *14*, 456. [[CrossRef](#)]
22. Bridge, J.S. The interaction between channel geometry, water flow, sediment transport and deposition in braided rivers. In *Braided Rivers*; Best, J.L., Bristow, C.S., Eds.; Geological Society of London: London, UK, 1993.
23. Alexander, J. A discussion on the use of analogues for reservoir geology. In *Advances in Reservoir Geology*; Ashtonm, M., Ed.; Geological Society of London: London, UK, 1992.
24. Bristow, C.S.; Best, J.L. Braided rivers: Perspectives and problems. In *Braided Rivers*; Best, J.L., Bristow, C.S., Eds.; Geological Society of London: London, UK, 1993.
25. Zhang, X.; Han, L.; Robinson, M.; Gallagher, A. A Gans-Based Deep Learning Framework for Automatic Subsurface Object Recognition From Ground Penetrating Radar Data. *IEEE Access* **2021**, *9*, 39009–39018. [[CrossRef](#)]
26. Bornik, A.; Neubauer, W. 3D Visualization Techniques for Analysis and Archaeological Interpretation of GPR Data. *Remote Sens.* **2022**, *14*, 1709. [[CrossRef](#)]
27. Mitchum, R.M.; Vail, P.R.; Sangree, J.B. Seismic stratigraphy and global changes of sea-level, Part 6: Stratigraphic interpretation of seismic reflection patterns in depositional sequences. In *Seismic Stratigraphy—Applications to Hydrocarbon Exploration*; Payton, C.E., Ed.; AAPG Memoir: Tulsa, OK, USA, 1977; Volume 26, pp. 117–133.
28. Roksandic, M.M. Seismic facies analysis concepts. *Geophys. Prospect.* **1978**, *26*, 383–398. [[CrossRef](#)]
29. Sangree, J.B.; Widmier, J.M. Interpretation of depositional facies from seismic data. *Geophysics* **1979**, *44*, 131–160. [[CrossRef](#)]
30. Brierley, G.J. Channel morphology and element assemblage: A constructivist approach to facies modeling. In *Advances in Fluvial Dynamics and Stratigraphy*; Carling, P.A., Dawson, M.R., Eds.; Wiley: Chichester, UK, 1996; pp. 263–298.
31. Miall, A.D. Architectural-element analysis: A new method of facies analysis applied to fluvial deposits. *Earth-Sci. Rev.* **1985**, *22*, 261–308. [[CrossRef](#)]
32. Miall, A.D. Architecture and sequence stratigraphy of Pleistocene fluvial systems in the Malay Basin, based on seismic time-slice analysis. *Am. Assoc. Pet. Geol. Bull.* **2002**, *86*, 1201–1216.
33. Allen, J.R.L. Studies in fluvial sedimentation: Bars, bar-complexes and sandstone sheets (low-sinuosity braided streams) in the Brownstones (L. Devonian), Welsh Borders. *Sediment. Geol.* **1983**, *33*, 237–293. [[CrossRef](#)]
34. Cant, D.J.; Walker, R.G. Fluvial processes and facies sequences in the sandy braided South Saskatchewan River, Canada. *Sedimentology* **1978**, *25*, 625–648. [[CrossRef](#)]
35. Miall, A.D. *The Geology of Fluvial Deposits. Sedimentary Facies, Basin Analysis, and Petroleum Geology*; Springer: Berlin/Heidelberg, Germany, 1996.
36. Hjøllbakk, A. Facies and fluvial architecture of a high-energy braided river: The Upper Proterozoic Seglommen Member, Varanger Peninsula, northern Norway. *Sediment. Geol.* **1997**, *114*, 131–160. [[CrossRef](#)]
37. Bridge, J.S.; Lunt, I.A. Depositional models of braided rivers. In *Braided Rivers: Processes, Deposits, Ecology and Management*; Sambrook Smith, G.H., Best, J.L., Bristow, C.S., Petts, G.E., Eds.; International Association of Sedimentologist, Special Publications: Algiers, Algeria, 2009; Volume 36, pp. 11–50.
38. Miall, A.D. Reservoir heterogeneities in fluvial sandstones: Lessons from outcrop studies. *Am. Assoc. Pet. Geol. Bull.* **1988**, *72*, 682–697.
39. DU, P. Structure characteristic and relations with neighbouring area in Datong coalfield. *Geol. Rev.* **1964**, *22*, 259–266.
40. Yu, X.H.; Ma, X.X.; Qing, H.R. Sedimentology and reservoir characteristics of a Middle Jurassic fluvial system, Datong Basin, northern China. *Bull. Can. Pet. Geol.* **2002**, *50*, 105–117. [[CrossRef](#)]
41. Chen, Y.X.; Dai, D.L. Depositional facies of Jurassic in Datong area, Shanxi province. *Acta Geol. Sin.* **1962**, *42*, 321–338.
42. Shunli, L.; Xinghe, Y.; Bintao, C. Quantitative Characterization of Architecture Elements and Their Response To Base-Level Change In A Sandy Braided Fluvial System At A Mountain Front. *J. Sediment. Res.* **2015**, *85*, 1258–1274. [[CrossRef](#)]
43. Culbertson, J.K.; Scott, C.H. Sandbar development and movement in an alluvial channel. *Rio Gd. Near Bernado N. M. US Geol. Surv. Prof. Pap.* **1970**, *700*, 237–241.
44. Ardies, G.W.; Dalrymple, R.W.; Zaitlin, B.A. Controls on the geometry of incised valleys in the Basal Quartz unit (Lower Cretaceous), Western Canada Sedimentary Basin. *J. Sediment. Res.* **2002**, *72*, 602–618. [[CrossRef](#)]

45. Bolla Pittaluga, M.; Repetto, R.; Tubino, M. Channel bifurcation in braided rivers: Equilibrium configurations and stability. *Water Resour. Res.* **2003**, *39*, 1–13. [[CrossRef](#)]
46. Best, J.L.; Ashworth, P.J.; Bristow, C.S.; Roden, J. Three-dimensional sedimentary architecture of a large, mid-channel sand braid bar, Jamuna River, Bangladesh. *J. Sediment. Res.* **2003**, *73*, 516–530. [[CrossRef](#)]
47. Bluck, B.J. Sedimentation in some Scottish rivers of low sinuosity. *Trans. R. Soc. Edinb. Earth Sci.* **1976**, *69*, 425–456. [[CrossRef](#)]
48. Skelly, R.L.; Bristow, C.S.; Ethridge, F.G. Architecture of channel-belt deposits in an aggrading shallow sandbed braided river: The lower Niobrara River, northeast Nebraska. *Sediment. Geol.* **2003**, *158*, 249–270. [[CrossRef](#)]
49. Lunt, I.A.; Smith, G.H.S.; Best, J.L.; Ashworth, P.J.; Lane, S.N.; Simpson, C.J. Deposits of the sandy braided South Saskatchewan River: Implications for the use of modern analogs in reconstructing channel dimensions in reservoir characterization. *Am. Assoc. Pet. Geol. Bull.* **2013**, *97*, 553–576. [[CrossRef](#)]
50. Miall, A.D. Reconstructing the architecture and sequence stratigraphy of the preserved fluvial record as a tool for reservoir development: A reality check. *Am. Assoc. Pet. Geol. Bull.* **2006**, *90*, 989–1002. [[CrossRef](#)]
51. Aragon, B.; Johansen, K.; Parkes, S.; Malbeteau, Y.; Al-Mashharawi, S.; Al-Amoudi, T.; McCabe, M.F. A calibration procedure for field and UAV-based uncooled thermal infrared instruments. *Sensors* **2020**, *20*, 3316. [[CrossRef](#)] [[PubMed](#)]